High-throughput exploration of alloying as design strategy for thermoelectrics

Sandip Bhattacharya and Georg K. H. Madsen
ICAMS, Ruhr-Universität Bochum, 44780 Bochum, Germany
(Received 3 July 2015; published 27 August 2015)

We explore a material design strategy to optimize the thermoelectric power factor. The approach is based on screening the band structure changes upon a controlled volume change. The methodology is applied to the binary silicides and germanides. We first confirm the effect in antifluorite Mg_2Si and Mg_2Ge where an increased power factor by alloying with Mg_2Sn is experimentally established. Within a high-throughput formalism we identify six previously unreported binaries that exhibit an improvement in their transport properties with volume. Among these, hexagonal $MoSi_2$ and orthorhombic Ca_2Si and Ca_2Ge have the highest increment in zT with volume. We then perform supercell calculations on special quasirandom structures to investigate the possibility of obtaining thermodynamically stable alloy systems which would produce the necessary volume changes. We find that for Ca_2Si and Ca_2Ge the solid solutions with the isostructural Ca_2Sn readily forms even at low temperatures.

DOI: 10.1103/PhysRevB.92.085205 PACS number(s): 84.60.Rb, 72.15.Jf, 31.15.A−, 79.10.−n

I. INTRODUCTION

Despite their importance, the discovery of new materials is often based on trial and error. High-throughput (HT) computational screening [1,2] is an important step towards identifying materials with desired properties in a more systematic way. Thermoelectric (TE) materials are attractive for such computational searches because continuous development of computational methodology means that all parts of the TE figure of merit, zT can in principle be calculated from first principles [3–6]. In practice, computational HT searches for new TE materials have focused on parts of the $zT = S^2\sigma T/\kappa$, where S is the Seebeck coefficient, σ the electrical, and κ the thermal conductivity [7–11]. Despite this, there are now a few works where computational screening has led to high-performance TE materials that could be experimentally realized [12–15].

Beyond screening known compounds, there still exists great challenges designing new materials with specific properties. This is especially the case for electronic structure-dependent properties, which have highly nontrivial dependencies on the atomic structure [16]. For TE materials one strategy for designing new alloys with optimized properties is by a controlled volume change. We label this procedure volumetric band structure alignment (VBA). The idea is illustrated in Fig. 1, where the energy dependence of two bands vary differently upon a change of volume. Thereby a scenario can occur when the band edges are aligned, as schematically illustrated in the middle panel of Fig. 1. How this optimizes the TE power factor, $PF = S^2\sigma$, can be understood by considering the generalized transport coefficients,

$$\mathcal{L}^{(\alpha)} = q^2 \int \sigma(\varepsilon)(\varepsilon-\mu)^{\alpha}\left(-\frac{\partial f}{\partial \varepsilon}\right)d\varepsilon, \tag{1}$$

where f is the Fermi distribution and $\sigma(\varepsilon)$ the transport distribution. The Seebeck and electric conductivity are given as $S = \mathcal{L}^{(1)}/qT\mathcal{L}^{(0)}$ and $\sigma = \mathcal{L}^{(0)}$, respectively. For two channels (labeled $'$ and $''$) conducting in parallel, $\mathcal{L}^{(\alpha)}$ is given as the sum of the contributions from each channel, so that the PF is,

$$S^2\sigma = \frac{1}{q^2T^2}\frac{(\mathcal{L}^{(1)'}+\mathcal{L}^{(1)''})^2}{\mathcal{L}^{(0)'}+\mathcal{L}^{(0)''}}. \tag{2}$$

Without loss of generality we can write $\mathcal{L}^{(1)''} = \alpha_1\mathcal{L}^{(1)'}$ and $\mathcal{L}^{(0)''} = \alpha_0\mathcal{L}^{(0)'}$. Thereby it is clear that the PF will be increased if,

$$(1+\alpha_1)^2 > 1+\alpha_0. \tag{3}$$

$\mathcal{L}^{(1)}$ and thereby S will be significant when the chemical potential is located within the relatively narrow energy window defined by $\partial f/\partial\varepsilon$ of a band edge. Aligning band edges with similar effective masses within $\partial f/\partial\varepsilon$, will satisfy Eq. (3) and lead to an increased PF when compared to the largest of the individual contributions. Such band structure characteristics are found in several materials with complex carrier pocket shapes, which results in enhanced TE properties [17–20].

VBA has been successfully applied to optimize the PF in the n-doped $Mg_2Si_{1-x}Sn_x$ (and $Mg_2Ge_{1-x}Sn_x$) and in p-doped $PbTe_{1-x}Se_x$ alloys [21,22]. In both the cases the volume was controlled by alloying. Consider as an example the alloy composition $MX_{1-x}X'_x$. According to Vegard's law, the volume of the resulting alloy system, will be directly proportional to the fraction of the new composition added, i.e., x. The volume will also be influenced by the thermal expansion, and this together with alloying offers the possibility to control the peak temperature of TE performance [23].

The question whether it is possible to optimize the band structure by VBA for a given compound is very difficult to answer from intuition alone. It depends on the detailed band structure and how the different bands react to a volume change. The effect of VBA can be strongly affected by changes to the band gap and doping level. Furthermore, it can be very difficult to predict whether a given compound can be alloyed or not. For example, while a solid solution of Si and Sn in $Mg_2Si_{1-x}Sn_x$ can form even at low temperatures [24–27] it is well known that Sn is hardly soluble in diamond-Si.

The idea behind the present work is to explore a HT computational strategy to identify systems where VBA can be applied. The approach is based on screening the volumetric effect on the band structure and calculate *ab initio* thermodynamics to asses the possibility of alloying. It is shown that systems allowing VBA are quite rare and that the procedure leads to a very strong screening of potential candidates. We focus on the electronic part of the zT. However, alloying will also be advantageous in terms of reducing

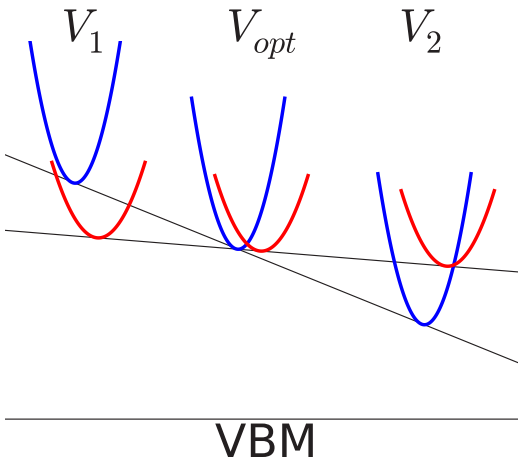

FIG. 1. (Color online) Schematic illustration of volumetric band alignment for a n-type material. VBM stands for the valence band minimum.

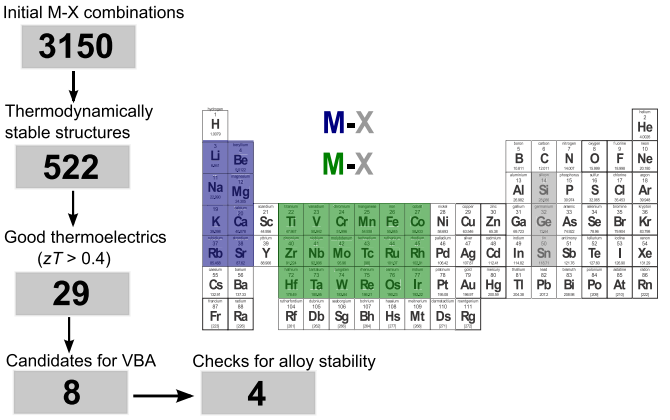

FIG. 2. (Color online) Flowchart of the HT procedure employed to investigate the candidates for volumetric band engineering. The criterion for good thermoelectrics, i.e., $zT > 0.4$, within our scheme is checked at $T = 600$ K and $n = 2 \times 10^{20}\text{cm}^{-3}$ with zT evaluated from Eq. (4).

the thermal conductivity either by lowering mass disorder scattering or by using natural solubility limits to nanostructure the material [28].

We will explore binary alloys of the group 14 elements. Silicon is the second most abundant element on the Earth's crust [29] making such systems quite attractive. Stable alloys and solid solutions with optimized electronic structures and transport properties have been realized with many binary silicides plus the corresponding germanides or stannides compounds [21]. While Ge and Sn are not as abundant and cheap as Si, they are certainly not rare elements either [30]. Other crucial advantages that these M-Si/Ge/Sn alloy systems enjoy, is the ease with which they can be doped. Indeed, silicide group compounds exhibit a high density of mobile charge carriers upon doping of up to $n = 10^{20}$–10^{21}cm^{-3}. Furthermore, they often have high melting points making them attractive stable candidates for high T TE [31].

II. METHODS

A. High-throughput scheme

Our HT scheme is illustrated in Fig. 2. We consider binary M-X systems, where M is a metal taken to be a $3d$, $4d$, or $5d$ transition metals (TM) or $2s$, $3s$, and $4s$ alkali (A) or alkaline earth (AE) metals and X is Si, Ge or Sn. The first step of our work is to identify the stable structures in the constituent binary system. The phase stability is evaluated within a high-throughput formalism based on our previous works [10]. For each metal silicide (or germanide) combination, the crystal structures were relaxed and the formation energy was calculated. The candidate structures were generated by the extracting the known structures from the Pearson's database [32] and appropriate substitution of the known structures with similar atoms (in same group of Periodic Table). Furthermore, we have also incorporated the silicides structures from our previous work [10] and consequent substitution of similar atoms.

In total, we have investigated 3150 different compounds. For a given M-X binary system, we select the structures that have the difference in formation energies from the corresponding convex hull, ΔE_h, lower than 50 meV/atom. The $\Delta E_h < 50$ meV/atom tolerance has statistically been shown to contain 80% of the experimentally known compounds in the TM-Si system [10] and narrows the original number to 522 thermodynamically stable compounds, Fig. 2.

Thereafter, the self-consistent calculations for these selected structures were performed using the (L)APW+lo method [33] implemented within the WIEN2K code. [34]. These were followed by band structure calculations on a finer k-mesh of $\frac{64\times10^6}{V_{\text{unitcell}}}$ k-points in the full Brillouin zone (BZ). All calculations in this work are reported for Perdew-Burke-Ernzerhof (PBE) [35] exchange-correlation potential. Subsequently, the electronic transport properties were evaluated using the BOLTZTRAP code [36]. The code evaluates the Seebeck coefficient on an absolute scale and electrical conductivity in terms of the carrier relaxation time τ using the rigid band approximation. To evaluate the potential for TE energy conversion we utilize a modified version of the definition of figure of merit, zT,

$$zT = \frac{S^2 \frac{\sigma}{\tau} T}{L_o \frac{\sigma}{\tau} T + \frac{\kappa_{\text{ph}}}{\tau}}, \tag{4}$$

The denominator in Eq. (4) accounts for the total thermal conductivity of the material, with its electronic part, $\kappa_{\text{el}} = L_o \frac{\sigma}{\tau} T$, written according to the Wiedemann-Franz law. Here L_o is the Lorenz number, $L_o = 2.44 \times 10^{-8}\,\text{W}\,\Omega\,\text{K}^{-2}$. Finally the phononic part of thermal conductivity is κ_{ph}. All the transport quantities in Eq. (4) are extracted on an absolute scale, apart from $\frac{\kappa_{\text{ph}}}{\tau}$, which is set at $10^{14}\,\text{W}\,\text{K}^{-1}\,\text{ms}^{-1}$ [7]. In reality, the magnitude of $\frac{\kappa_{\text{ph}}}{\tau}$ will be dictated by both intrinsic properties such as the phonon band structure and phonon- and electron-phonon coupling and by the details of sample preparation control, e.g., grain size (nanostructuring) or the existence of multiple phases. zT, as defined in Eq. (4), epitomizes the electronic contribution to the TE performance and has been validated in the prediction of TE materials [7,10,17]. It can be viewed as a descriptor for identifying potential high TE performance under the assumption of a low thermal

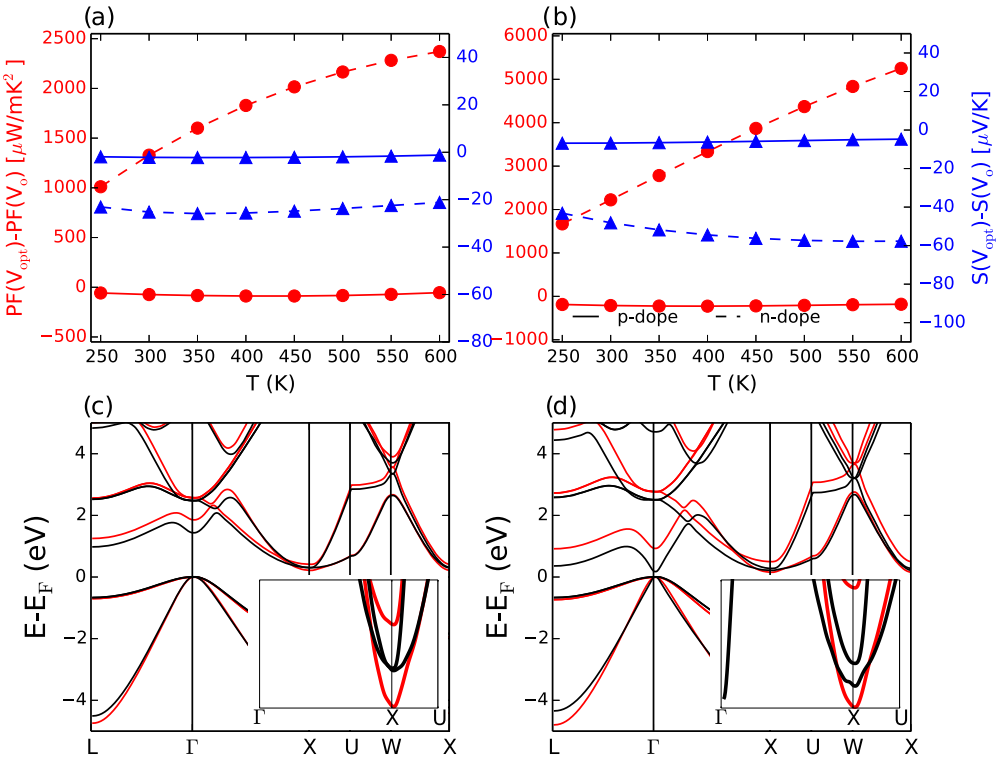

FIG. 3. (Color online) Volumetric band alignment in Mg_2X. (a) and (b) respectively show the change in $PF(V_{opt}) - PF(V_0)$ (in red circles) and $S(V_{opt}) - S(V_0)$ (blue triangles), as a function of temperature at $n = 2 \times 10^{20}\text{cm}^{-3}$. Furthermore, in both the graphs the dashed lines correspond to n doping while the bold line represents the data for the p-doping scenario. (c) and (d) respectively show the band structures for Mg_2Si and Mg_2Ge, at V_0 (red) and V_{opt} (black). The insets represent the zoomed view of the conduction band minimum. The conventions used in this figure will be used in the forthcoming figures presenting similar results for other candidates in this paper.

conductivity, a long electron lifetime and the possibility of reaching the optimal doping. Setting a criteria of $zT > 0.4$ [evaluated using Eq. (4)] at $T = 600$ K and 2×10^{20} cm^{-3} reduces the number of potential candidates to 29.

The procedure was then repeated at unit cell volumes in the $\pm 7\%$ range of the equilibrium volume. The volume dependence of the descriptor, i.e., $zT(V)$, is evaluated and we identify zT_{opt} and zT_0, which are the magnitude of zT at the volume, which maximizes $zT(V)$ and at the calculated equilibrium volume respectively. Thus, for any given material, if $\frac{zT(V_{opt})}{zT(V_0)} > 1.1$, it will be of interest for the purpose of this work. As can be seen in Fig. 2 this lowers the number of candidate structures to only eight.

The final step is to consider whether the volume change by alloying is thermodynamically feasible. Consider a mixture of $1 - x$ mole fractions of the binary AB_n and x mole fractions of the binary AC_n producing the alloy $AB_{n-x}C_x$. The excess energy that is required to obtain the alloy, also referred to as the mixing energy, is

$$\Delta E_{\text{mix}}(x; \text{AB}_n, \text{AC}_n) = \Delta E_f(AB_{n-x}C_x) - \frac{x\Delta E_f(AC_n) + (n-x)\Delta E_f(AB_n)}{n}, \quad (5)$$

where ΔE_f are the formation energies per atom for the given compounds. We have calculated the mixing energies from Eq. (5), by taking special quasirandom structure (SQS) alloy distributions for different values of x using the ATAT code [37]. For solids, since at ambient pressures, $P\Delta_{\text{mix}}V$ term is negligible, the enthalpy of mixing can be approximated as $\Delta H_{\text{mix}} = \Delta E_{\text{mix}}$. Thus the mixing Gibbs free energy is,

$$\Delta G_{\text{mix}}(x) = \Delta E_{\text{mix}}(x) + \frac{RT}{n+1}[x \ln x + (1-x)\ln(1-x)], \quad (6)$$

where, the last term accounts for entropy of mixing. For each of the alloys, the minimum temperatures, at which the entropy gain in alloy formation compensates the energy cost of mixing, can be obtained by minimizing Eq. (6). We will report T_m, which is the maximum temperature of the boundary of corresponding miscibility. As will be discussed later, this in the end limits the number of potential candidates to only four.

B. Identifying Mg_2X as a promising candidate

In the following we will introduce the HT scheme by example, using the $Mg_2Si/Ge/Sn$ system, which is well known for its potential VBA [21]. In the top panel of Fig. 3, the temperature dependence of the enhancement of the TE properties upon volume optimization, i.e., $PF(V_{opt}) - PF(V_0)$ and $S(V_{opt}) - S(V_0)$ for the antifluorite structure of Mg_2Si [Fig. 3(a)] and Mg_2Ge [Fig. 3(b)] are shown at a doping of $n = 2 \times 10^{20}\,\text{cm}^{-3}$. In the bottom panel Fig. 3(c), the band structures for Mg_2Si at equilibrium volume and the optimized

TABLE I. Summary of eight candidates that exhibit the VBA effect. We summarize zT_{opt} and zT_{opt}/zT_0 magnitudes at doping of $n = 2 \times 10^{20}$cm^{-3} and $T = 600$ K. The distance from the convex hulls, ΔE_h [ΔE_h^{Sn}] of the candidate (alloying possibility), carrier sign and V_{opt} (expressed as an increment from V_0) are also summarized.

Compound	zT_{opt}	zT_{opt}/zT_0	ΔE_h [ΔE_h^{Sn}] (meV/atom)	doping	V_{opt} (%)
Mg_2Si	1.07	1.33	0[0]	n	2.0
Mg_2Ge	1.17	2.19	0[0]	n	5.0
Ca_2Si	0.80	1.33	0[0]	n	5.0
Ca_2Ge	0.81	1.25	0[0]	n	2.5
Ca_9Ge_5	0.96	1.47	37.4[17.9]	p	6.1
β-$MoSi_2$	0.77	1.75	27.3[180.8]	n	3.0
o-Fe_2Ge_3	0.47	1.19	0.1[22.5]	n	3.0
t-Fe_2Ge_3	0.54	1.38	0[22.8]	n	3.0

volume are plotted. Likewise, Fig. 3(d) illustrates the band structures at V_0 and V_{opt} for Mg_2Ge.

In Figs. 3(a) and 3(b) we observe that for the p-type behavior the change in PF with volume is negligible for all T. On the other hand, for n-type behavior, the PF shows a pronounced increase at the optimized volume for both the compounds, that further enhances with T. Moreover S also exhibits an increase. Note that for n doping, the higher the negative value of $S(V_{opt}) - S(V_0)$, the more is the desired enhancement of the thermopower and zT. Also, it is well known that Mg_2Si exhibits a persistent n-type conductivity under any kind of crystal growth conditions [38–40]. When we analyze the variation in the conduction bands (CB) of the compounds with volume [Figs. 3(c) and 3(d)], the large increment in the PFs for n-doped Mg_2Si and Mg_2Ge becomes quite apparent. At the X point in the BZ near the conduction band minimum (CBM), the first and second CBs directly coincide at V_{opt} for Mg_2Si and are only a few meV apart for Mg_2Ge (see insets). Therefore, even at low dopings, the charge carriers (electrons) residing in both the bands will contribute to enhance the PF and Seebeck coefficient, as opposed to the contributions coming from electrons in only a single band, at equilibrium volume.

For Mg_2Si, at a doping of $n = 2 \times 10^{20}$ cm^{-3} and $T = 600$ K, the highest increment in zT is observed at volume increase of 2% from the equilibrium volume, Table I. According to Vegard's law this corresponds roughly to alloying Mg_2Si with 10% Mg_2Sn. This value will also be dependent on the carrier concentration and temperature at which the transport properties are calculated. The important rule is if a large VBA effect is observed at a small volume change that in principle can be attained by alloying. The second crucial criterion is whether the alloying is thermodynamically feasible. The energy of formation vs volume for $Mg_2X_{1-x}Y_x$ solid solution is depicted in Fig. 4. Here X is Si or Ge while Y is Ge or Sn. It can be seen that the excess mixing energy required for the formation of stable alloys is small in magnitude. As a result the optimal Sn content can be reached at moderate growth temperature, Fig. 4 inset. ΔE_{mix} and T_m are in good agreement with previous DFT calculation [24], especially considering that we employ a somewhat different computational approach using SQS based supercells and linear interpolation between

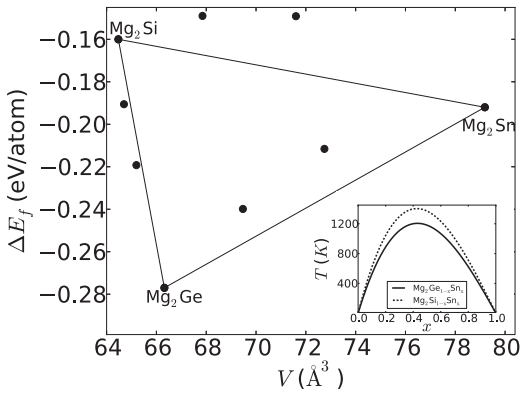

FIG. 4. Formation energy vs volume for $Mg_2X_{1-x}Y_x$ alloys. Here X, Y are Si, Ge, and Sn. The insert shows the miscibility gap calculated by minimizing Eq. (6).

the calculated points when minimizing Eq. (6). We also find a good agreement with CALPHAD and experimental results for this system [25–27].

Thus in the particular cases of antifluorite Mg_2Si and Mg_2Ge, the VBA can be conveniently achieved through alloying. While $Mg_2Si_{1-x}Ge_x$ alloy thermodynamically exists as a solid solution even at low temperatures, for $Mg_2Si_{1-x}Sn_x$ and $Mg_2Ge_{1-x}Sn_x$ alloys the desired volume increment can be achieved at the expense of only a small magnitude of mixing energy [24–27].

III. RESULTS AND DISCUSSION

A. Electronic screening

Based on the descriptors discussed above other candidates for VBA effect will now be identified. The top and bottom panels in Fig. 5 illustrates zT_{opt} vs zT_0 respectively for all silicides and germanides, at a doping of $n = 2 \times 10^{20}$ cm^{-3} and $T = 600$ K. Each data point in Fig. 5 represents a particular compound.

Thus Fig. 5 contains three vital descriptors to identify candidates for VBA: (i) the magnitude of zT_0, which indicates if a particular candidate is a good TE material; (ii) the value $\frac{zT_{opt}}{zT_0}$, which helps us to identify the promising candidates exhibiting the volumetric enhancement of their TE properties; (iii) the magnitude of the distance from the corresponding convex hull of the possible alloying choices, which would produce the necessary volumetric change upon alloying (according to Vegard's law).

A summary of the promising silicide and germanide structures that exhibit a large VBA effect are shown in Table I, with the corresponding value of zT_{opt}, zT_{opt}/zT_0 and ΔE_h [ΔE_h^{Sn}]. Eight such compounds were identified to exhibit encouraging VBA effects upon using the magnitude of zT_{opt}/zT_0 and ΔE_h as descriptors.

In general, with increasing doping we observe that more number of candidates show the VBA effect. This is due to a large value of zT itself that is improved upon doping. However the best candidates, as listed in Table I, exhibiting VBA remained unchanged. Apart from Mg_2Si and Mg_2Ge, discussed previously, orthorhombic Ca_2Si and Ca_2Ge, hexagonal Ca_9Ge_5 and hexagonal $MoSi_2$ show encouraging results.

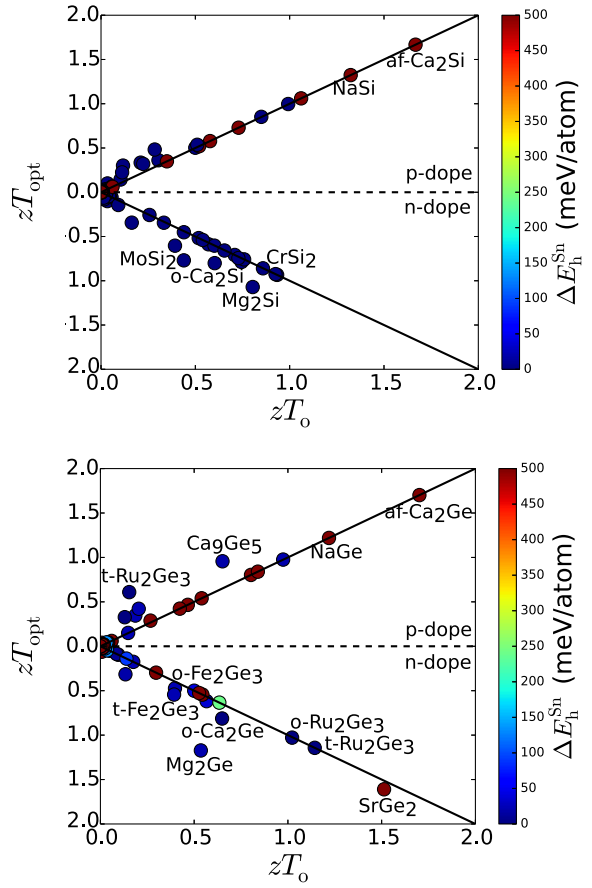

FIG. 5. (Color online) $zT_{\rm opt}$ vs $zT_{\rm o}$ for all silicides (top) and germanides (bottom) at doping $n = 2 \times 10^{20}{\rm cm}^{-3}$ and $T = 600$ K. Furthermore, the scatter points are colored based on the distance from the convex hull, $\Delta E_{\rm h}^{\rm Sn}$, of the corresponding Sn compound with the same structure as the host binary. For example, in the case of the Ca_9Ge_5 compound, $\Delta E_{\rm h}$ of the corresponding isostructural Ca_9Sn_5 is used for the color code, and so on. The candidates that exhibit VBA, $\frac{zT_{\rm opt}}{zT_0} > 1.1$, or have a large value of zT_0 are labeled. Also, if a compound crystallizes in more than one phase, the corresponding structure is also indicated with a prefix *o-* for orthorhombic, *t-* for tetragonal, and *af-* for antifluorite phase.

Note that in Fig. 5 there are compounds that show very little to no VBA effect but exhibit large zT_0. Indeed, despite our semiempirical determination of zT, we correctly predict most of these binaries with large values of zT_0, that are already established as encouraging TE materials [31]. Compounds which exhibit zT_0 in excess of 1.0, at $n = 2 \times 10^{20}$ carriers per cm^{-3}, are the orthorhombic and tetragonal structures of Ru_2Ge_3, cubic RuSi (at low temperatures), and tetragonal NaGe and NaSi. Furthermore, the following compounds have zT_0 between 0.5 and 1.0 (not listed in Fig. 5): hexagonal $CrSi_2$, Mn_4Si_7, $FeSi_2$, $ReSi_{1.75}$, and CoSi.

B. Feasibility in alloying

We will now explore the possibility of forming thermodynamically stable alloys among the candidates for VBA, identified based on the descriptors discussed so far. These alloys are summarized in Table II together with proportion of alloying component $x_{\rm alloy}$ required to produce the highest optimized PFs in the candidates. Note that the optimal VBA for most candidates are achieved at $x \leqslant 0.30$.

TABLE II. Alloy thermodynamics of the candidates. $x_{\rm alloy}$ is the amount of alloying component, calculated using Vegard's law, required to obtain the volume change for the VBA effect. $\Delta E_{\rm mix}(x = 0.25)$ is the mixing energy required to form the alloy (at $x = 0.25$). T_m is the maximum temperature of the boundary of the miscibility gap and $x(T = 800$ K) is the amount of alloying component which can be accommodated at $T = 800$ K in the alloy.

Alloys	$x_{\rm alloy}$	$\Delta E_{\rm mix}(x = 0.25)$ (kJ/mol.atom)	T_m (K)	x ($T = 800$ K)
$Mg_2Si_{1-x}Sn_x$	0.09	1.997	1281	0.171
$Mg_2Ge_{1-x}Sn_x$	0.26	1.595	1023	0.138
$Ca_2Si_{1-x}Sn_x$	0.30	0.013	78	all
$Ca_2Ge_{1-x}Sn_x$	0.18	0.015	97	all
$Ca_9Ge_{5-x}Sn_x$	0.28	4.495	>5000	0.019
β-$MoSi_{2-x}Sn_x$	0.07	30.980	>5000	0.008
o-$Fe_2Ge_{3-x}Sn_x$	0.10	32.746	>5000	0.004
t-$Fe_2Ge_{3-x}Sn_x$	0.10	29.681	>5000	0.005

In the previous section we have established that Ca_2Si and Ca_2Ge are attractive candidates for VBA effect based on the descriptors, which characterize their transport properties. In Fig. 6, we illustrate the energy of formation of orthorhombic $Ca_2X_{1-x}Y_x$ solid solutions as a function of volume. We observe that for $x = 0.25$ and $x = 0.5$, the SQS generated random structures are actually lower in energy in comparison to the parent structures. We therefore generated all the possible ordered structures of $Ca_{64}Si_{24}Sn_8$ and $Ca_{64}Si_{16}Sn_{16}$ within a $2 \times 2 \times 2$ supercell. We found a previously unreported ordered structure in which the Sn atoms order along the short **b** axis to be marginally lower in energy in comparison to the random SQS structure chosen. Figure 7 illustrates this ordered structure, which can be thought of as being stabilized by Sn-Sn bonding along the short axis of the orthorhombic cell and by the shortest Sn-Sn distance within the unit cell. In Table II the energy difference between the ordered and disordered alloy is reported as $\Delta E_{\rm mix}$. The energy difference is very low and the alloying necessary to obtain the desired volume increment should be readily achieved through $Ca_2Si_{1-x}Sn_x$ and $Ca_2Ge_{1-x}Sn_x$ alloys. Thus Ca_2Si and Ca_2Ge

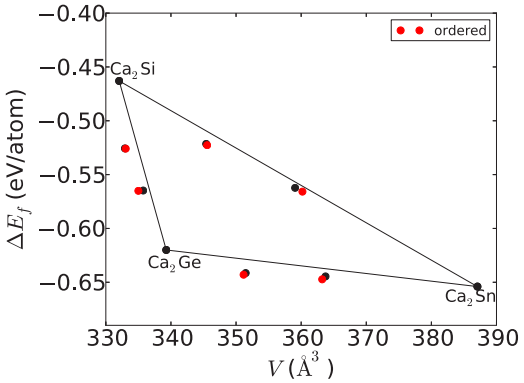

FIG. 6. (Color online) Formation energy vs volume for $Ca_2X_{1-x}Y_x$ solid solutions (X and Y are Si, Ge, and Sn).

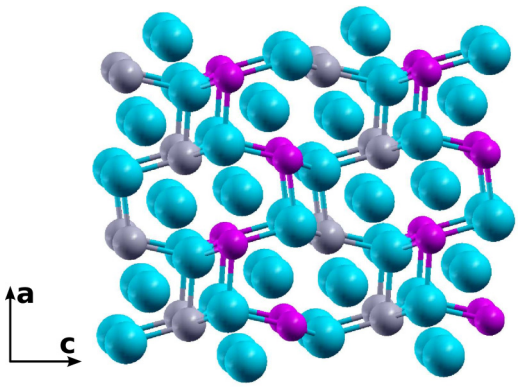

FIG. 7. (Color online) Ordered alloy structure is shown here for a $2 \times 2 \times 2$ supercell. Here the blue balls are Ca atoms, the grey balls are X atoms and the magenta ones are Y atoms. Note that an unit cell contains 12 atoms, i.e., $Ca_8X_2Y_2$ composition. The shortest crystallographic axis, **b**, is perpendicular to the plane. This structure is related to the Co_2Si (or TiNiSi) structure type with space group $Pnma$ [41].

compounds are confirmed to exhibit the VBA effect and the required volume change can also be conveniently achieved through alloying. Interestingly, Ca_2Sn has been previously proposed [42] as a thermoelectric material.

Unfortunately for all the other alloys, we obtained the mixing energy ΔE_{mix} to be very large (see Table II). Therefore for Ca_9Ge_5, β-$MoSi_2$, o-Fe_2Ge_3, and t-Fe_2Ge_3, the optimal VBA volume cannot be expected to be attained by the simple alloy choices listed in Table II.

Interestingly, we observe that for all four alloys having a large $\Delta E_{\text{mix}}(x = 0.25)$ in Table II, the corresponding pure compounds are found above the convex hull, Table I. For example, in the case of β-$MoSi_2$ we had obtained that β-$MoSn_2$ is far from the convex hull (i.e., ≈ 180 meV/atom). This could indicate that ΔE_h^{Sn} in Fig. 3, can serve as a minimal requirement for the possibility of forming a stable alloy system. Such a descriptor could help to avoid the computationally more expensive SQS supercell calculations.

C. Origin of high $zT(V_{\text{opt}})$ in encouraging structures

In the following, we shall investigate the role played by the electronic structure on VBA effect for the candidates. The main focus will be put on $CaSi_2$ and $CaGe_2$ where it has been shown that the necessary volume expansion should be achieved by alloying. We will furthermore discuss β-$MoSi_2$ and Ca_9Ge_5. For these candidates, while the optimal VBA volume can not be attained by alloying, we point out that even a small volume increase generated from either alloying or thermal expansion could improve their transport properties through the VBA effect.

1. *Orthorhombic* Ca_2Si *and* Ca_2Ge

Both Ca_2X compounds show a large volumetric enhancement in their TE properties. The top panel in Fig. 8 illustrate

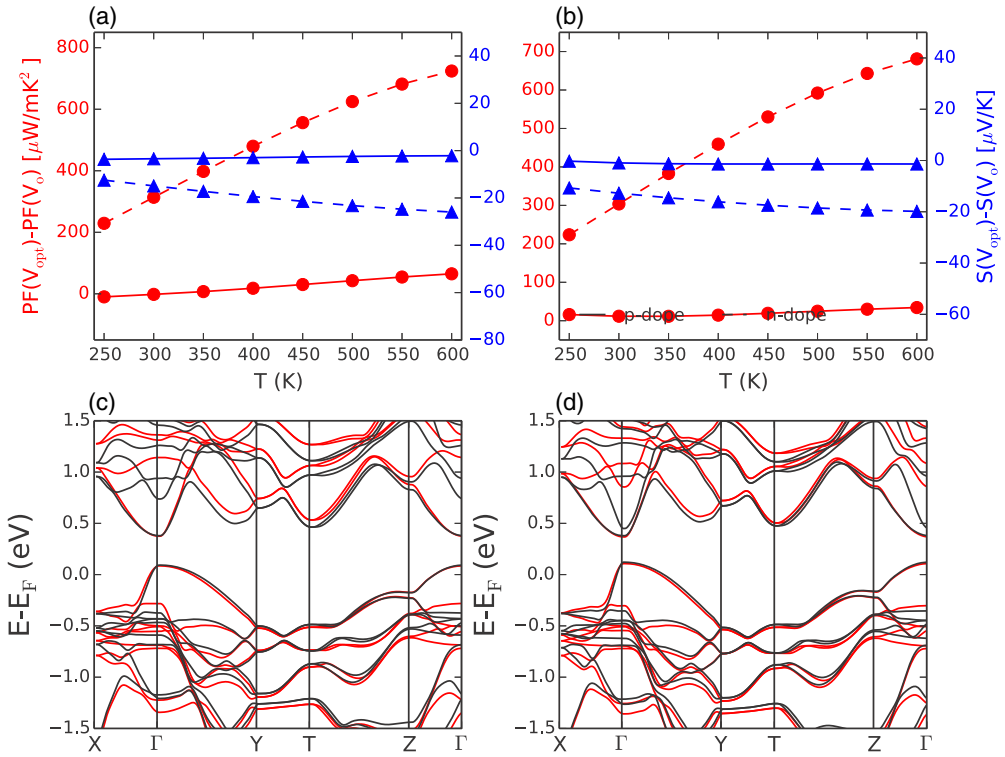

FIG. 8. (Color online) The temperature dependence of $PF(V_{\text{opt}}) - PF(V_0)$ and $S(V_{\text{opt}}) - S(V_0)$ for Ca_2Si and Ca_2Ge respectively in (a) and (b). Furthermore, in (c) and (d) we depict the corresponding band structures (V_{opt} in black and V_o in red; (c) for Ca_2Si and (d) for Ca_2Ge). The orthorhombic structure for these compounds are thermodynamically stable. Both the n-doped compounds exhibit an increase in PF and S that can be justified by the increased DOS around the CB manifold. Note also the close band alignment of the first two CBs at the Γ point in BZ, for Ca_2Ge.

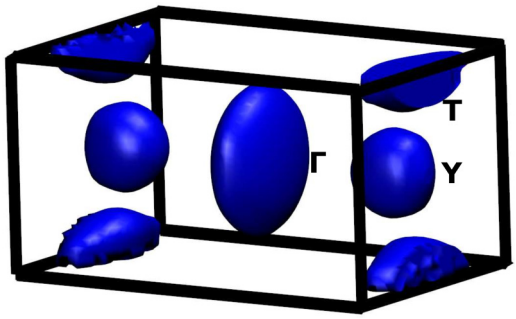

FIG. 9. (Color online) The BZ of orthorhombic Ca_2Si at V_{opt}, illustrating the electron pockets (in blue) at the high-symmetry T and Γ points as well as the low-symmetry pocket around Y. The electron pocket around the Y point does not exist at V_0.

the temperature dependance of the difference in PF (and S) between V_{opt} and V_0, for Ca_2Si in Fig. 8(a) and Ca_2Ge in Fig. 8(b). Likewise, the bottom panel shows the band structures of the two compounds [Fig. 8(c) for Ca_2Si and Fig. 8(d) for Ca_2Ge], at the two volumes.

The p-type behavior for both the compounds show a negligible amount of increase in PF and S at V_{opt}. Accordingly, the VBM, around the vicinity of Γ point, is relatively unchanged. The situation is different for the CBM, which has contributions coming from the Γ and T points at V_0. Due to this we have $zT_0^{Ca_2Si} = 0.60$ and $zT_0^{Ca_2Ge} = 0.64$, at $T = 600$ K and $n = 2 \times 10^{20}$ cm^{-3}. At optimal volume, n-type Ca_2Si and Ca_2Ge show an increase in their TE properties to $zT_{opt}^{Ca_2Si} = 0.80$ and $zT_{opt}^{Ca_2Ge} = 0.81$. From the band structures of Ca_2Si in Fig. 8(c), one can understand this volumetric enhancement. There is a lowering of the CBM at the T and around the Y point. This aligns several pockets close to the CBM edge, which is further illustrated in Fig. 9. The constant energy surface of the lowest conduction band of Ca_2Si at V_{opt} shows the electron pockets at the T and Γ points as well as those along the Γ-Y lines. The latter electron pocket does not exist at V_0. In the case of Ca_2Ge, a similar lowering of the lowest conduction band along the Γ-Y lines is observed in Fig. 8(d) at V_{opt}. Similar carrier pocket shapes have also been identified as the source of high σ in isostructural orthorhombic Ca_2Pb and Sr_2Pb [42].

2. *Hexagonal* Ca_9Ge_5

We shall now discuss the hexagonal structure of Ca_9Ge_5, which also exhibits an increase in its TE properties with volume change. In the same fashion as the data presented in the previous sections, Fig. 10(a) shows the temperature dependence of the change in PF and S at the two volumes, V_{opt} and V_0. The bottom panel shows the band structure at the two volumes.

The situation for Ca_9Ge_5 is quite interesting. Upon an increase in volume, there is an opening of the band gap at the Γ point in its BZ. This metal to semiconductor transition with volume change is the sole reason behind the enhancement of PF and S at V_{opt}, graphed in Fig. 10(b). Interestingly, a very high $zT_{opt}^{Ca_9Ge_5} = 0.96$ and $zT_{opt}/zT_0 = 1.47$ (at $T = 600$ K and $n = 2 \times 10^{20}$ cm^{-3}) was observed.

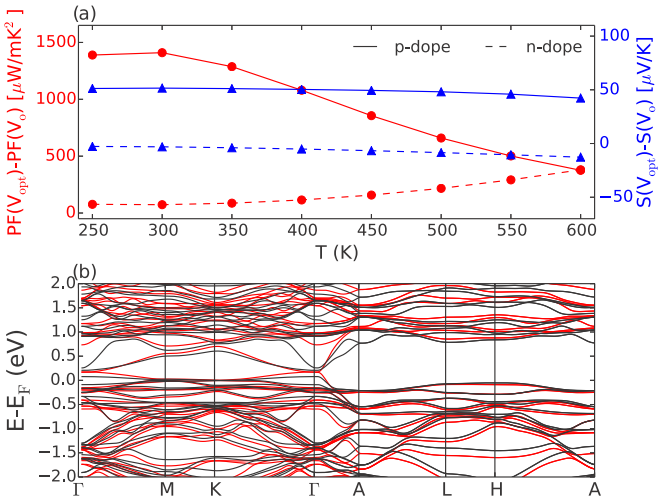

FIG. 10. (Color online) T dependence of $PF(V_{opt}) - PF(V_0)$ and $S(V_{opt}) - S(V_0)$ for the hexagonal Ca_9Ge_5 (top). The corresponding band structures at the two volumes are shown in the bottom panel. For Ca_9Ge_5, there is an opening of the band gap with volume change that is responsible for the increase in its PF and S.

3. *Hexagonal* $MoSi_2$

Molybdenum disilicide, $MoSi_2$, exists as α-$MoSi_2$, having a tetragonal body centered packing with a space group of $I4/mmm$ and as β-$MoSi_2$ that has a hexagonal closed packing arrangement with space group $P6_222$. Both the structures are composed of Mo and Si_2 layers in which Mo atoms are surrounded by six Si atoms. Both the allotropes of $MoSi_2$ exhibit properties such as high melting points, low resistivity, and high mechanical strength. While β-$MoSi_2$ is found to be 27.3 meV/atom above the convex hull, it can be conveniently synthesized from Mo and Si powders using

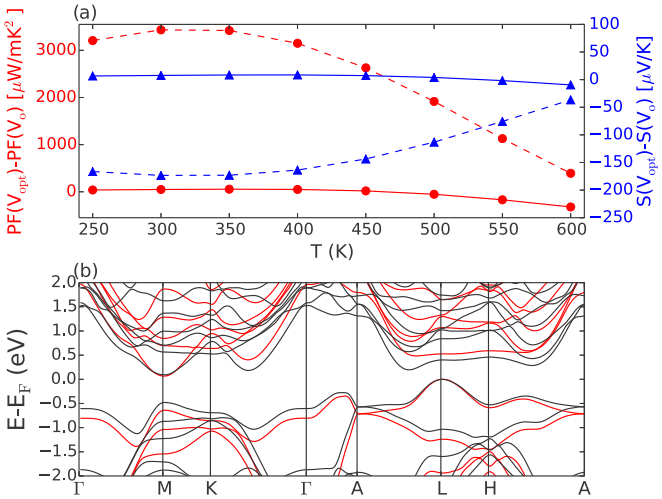

FIG. 11. (Color online) We depict the temperature dependence of $PF(V_{opt}) - PF(V_0)$ and $S(V_{opt}) - S(V_0)$ for the $\beta - MoSi_2$ in (a). In (b), we present the band structures at the two volumes (V_{opt} in black and V_o in red) for $\beta - MoSi_2$. n-type $MoSi_2$ shows an appreciable increase in both PF and S at V_{opt} up to $T = 350$ K. This increase can be explained by the lowering and aligning of the first CB manifold along multiple directions in its hexagonal BZ.

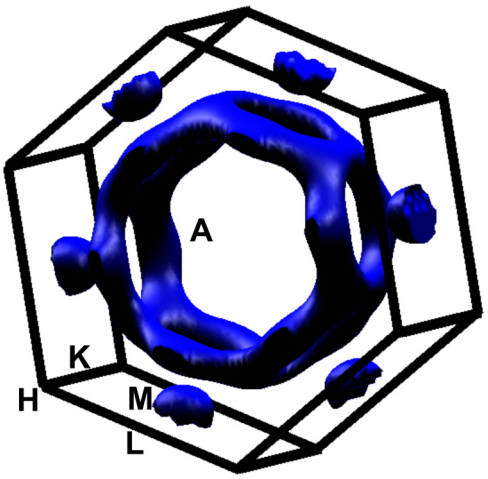

FIG. 12. (Color online) The BZ of β-$MoSi_2$ illustrating the Fermi surface at V_{opt}. We observe electronic contributions connecting several low symmetry points across the BZ in the Fermi surface, which is responsible for the VBA effect [also see Fig. 11(b)].

spark plasma sintering techniques [43,44], thus confirming the $\Delta E_h < 50$ meV/atom criteria. Moreover, since α-$MoSi_2$, which is extensively used in microelectronics, can be both p and n doped effectively, the same could be true for the less studied β phase.

Figure 11(a) shows the T dependence of difference in the thermoelectric properties (PF and S), between V_{opt} and V_0 for β-$MoSi_2$. Additionally, Fig. 11(b) shows the band structures at the two volumes. For n-doped $MoSi_2$ both the PF and S increases drastically by a volume expansion up to $T = 350$ K. The enhancement of PF and S is steadily reduced at temperatures above 350 K due to the small band gap. Please note that the results for all the candidates in Table I are presented at $T = 600$ K.

The explanation for the observed magnification in PF and S with volume, can be pinned down to the lowering in energy of the first CB, along multiple directions in its BZ observed in Fig. 11(b). These changes in the band structure not only causes an increased DOS of carriers around the CBM, but also an increased number of electron pockets. The Fermi surface demonstrating the electronic contributions at V_{opt} under doped scenario is shown in Fig. 12. Both the above discussed factors improve PF and S for n-doped $MoSi_2$ with volume enlargement. Consequently at a doping of $n = 2 \times 10^{20}$ cm^{-3}, we obtain the observe the largest VBA effect in this work of $zT_{opt}^{\beta\ MoSi_2} = 1.07$ and $zT_{opt}/zT_0 = 3.84$ (at $T = 450$ K) for n-doping scenario. The same values at $T = 600$ K are tabulated in Table. I.

IV. CONCLUSION

In this paper a computational HT scheme to identify compounds where the thermoelectric properties can be optimized by alloying is presented. We confirm that Mg_2Si and Mg_2Ge exhibit large enhancement of their thermoelectric properties with volume. We report that Ca_2Si and Ca_2Ge, hexagonal $MoSi_2$ and Ca_9Ge_5 could exhibit increased thermoelectric properties due to a volumetric band alignment. In the cases of Ca_2Si and Ca_2Ge the solid solutions with Sn can be obtained at the expense of a negligible amount of mixing energy and therefore the volume changes can be obtained by alloying. Among the remaining candidates, the volume increase for the VBA effect is thermodynamically difficult to achieve by alloying. However, we have obtained that β-$MoSi_2$ exhibits a significant increase in its thermoelectric properties due VBA, by the virtue of favorable changes to its band structure with volume. Thus, in this case even a small volume change due to alloying or thermal expansion may enhance its thermoelectric properties. Finally, we have established that ΔE_h^{Sn} can be a reliable descriptor to provide initial information on the stability of the corresponding alloys.

We have focused on systems where the electronic PF can be optimized with controlled volume changes. Alloying will also decrease the lattice part of the thermal conductivity, which will further improve the thermoelectric performance of the candidates.

ACKNOWLEDGMENTS

The authors would like to acknowledge funding from the Deutsche Forschungsgemeinschaft (DFG) Grants No. MA 5487/1-1 and No. MA 5487/4-1.

[1] S. Curtarolo, G. L. W. Hart, M. B. Nardelli, N. Mingo, S. Sanvito, and O. Levy, Nature Mater. **12**, 191 (2013).
[2] G. Hautier, A. Jain, and S. Ong, J. Mater. Sci. **47**, 7317 (2012).
[3] D. J. Singh and I. I. Mazin, Phys. Rev. B **56**, R1650 (1997).
[4] D. A. Broido, M. Malorny, G. Birner, N. Mingo, and D. A. Stewart, Appl. Phys. Lett. **91**, 231922 (2007).
[5] O. D. Restrepo, K. Varga, and S. T. Pantelides, Appl. Phys. Lett. **94**, 212103 (2009).
[6] B. Qiu, Z. Tian, A. Vallabhaneni, B. Liao, J. M. Mendoza, O. D. Restrepo, X. Ruan and G. Chen, Europhys. Lett. **109**, 57006 (2015).
[7] G. K. H. Madsen, J. Am. Chem. Soc. **128**, 12140 (2006).
[8] J. Yang, H. Li, T. Wu, W. Zhang, L. Chen, and J. Yang, Adv. Funct. Mater. **18**, 2880 (2008).
[9] S. Wang, Z. Wang, W. Setyawan, N. Mingo, and S. Curtarolo, Phys. Rev. X **1**, 021012 (2011).
[10] I. Opahle, A. Parma, E. J. McEniry, R. Drautz, and G. K. H. Madsen, New J. Phys. **15**, 105010 (2013).
[11] J. Carrete, W. Li, N. Mingo, S. Wang, and S. Curtarolo, Phys. Rev. X **4**, 011019 (2014).
[12] C. Bera, S. Jacob, I. Opahle, N. S. H. Gunda, R. Chmielowski, G. Dennler, and G. K. H. Madsen, Phys. Chem. Chem. Phys. **16**, 19894 (2014).
[13] S. Bhattacharya, N. S. H. Gunda, R. Stern, S. Jacobs, R. Chmielowski, G. Dennler, and G. K. H. Madsen, Phys. Chem. Chem. Phys. **17**, 9161 (2015).
[14] Q. Tan, L.-D. Zhao, J.-F. Li, C.-F. Wu, T.-R. Wei, Z.-B. Xing, and M. G. Kanatzidis, J. Mater. Chem. A **2**, 17302 (2014).

[15] G. Joshi, R. He, M. Engber, G. Samsonidze, T. Pantha, E. Dahal, K. Dahal, J. Yang, Y. Lan, B. Kozinsky, and Z. Ren, Energy Environ. Sci. **7**, 4070 (2014).
[16] J. Yan, P. Gorai, B. Ortiz, S. Miller, S. A. Barnett, T. Mason, V. Stevanovic, and E. S. Toberer, Energy Environ. Sci. **8**, 983 (2015).
[17] L. Bjerg, G. K. H. Madsen, and B. B. Iversen, Chem. Mat. **23**, 3907 (2011).
[18] X. Chen, D. Parker, and D. J. Singh, Sci. Rep. **3**, 3168 (2013).
[19] N. A. Mecholsky, L. Resca, I. L. Pegg, and M. Fornari, Phys. Rev. B **89**, 155131 (2014).
[20] D. S. Parker, A. F. May, and D. J. Singh, Phys. Rev. Applied **3**, 064003 (2015).
[21] V. K. Zaitsev, M. I. Fedorov, E. A. Gurieva, I. S. Eremin, P. P. Konstantinov, A. Y. Samunin, and M. V. Vedernikov, Phys. Rev. B **74**, 045207 (2006).
[22] Y. Pei, X. Shi, A. LaLonde, H. Wang, L. Chen, and G. Snyder, Nature (London) **473**, 66 (2011).
[23] Z. M. Gibbs, H. Kim, H. Wang, R. L. White, F. Drymiotis, M. Kaviany, and G. Jeffrey Snyder, Appl. Phys. Lett. **103**, 262109 (2013).
[24] R. Viennois, C. Colinet, P. Jund, and J.-C. Tèdenac, Intermetallics **31**, 145 (2012).
[25] I.-H. Jung, D.-H. Kang, W.-J. Park, N. J. Kim, and S. Ahn, Calphad **31**, 192 (2007).
[26] I.-H. Jung and N. J. Kim, J. Alloys Compounds **494**, 137 (2010).
[27] A. Kozlov, J. Gröbner, and R. Schmid-Fetzer, J. Alloys Compounds **509**, 3326 (2011).
[28] Q. Zhang, J. He, T. J. Zhu, S. N. Zhang, X. B. Zhao, and T. M. Tritt, Appl. Phys. Lett. **93**, 102109 (2008).
[29] *Mineral Commodity Summaries 2011* (U.S. Department of the Interior, U.S. Geological Survey: Reston, 2011); http://minerals.usgs.gov/minerals/pubs/mcs/2011/mcs2011.pdf
[30] http://www.chemicool.com/elements/
[31] M. Fedorov, J. Thermoelectricity **2**, 1607 (2009).
[32] Crystal Data: Crystal Structure Database for Inorganic Compounds (on CD-ROM) Release 2011/12 (ASM International Materials Park, 2012).
[33] G. K. H. Madsen, P. Blaha, K. Schwarz, E. Sjöstedt, and L. Nordström, Phys. Rev. B **64**, 195134 (2001).
[34] P. Blaha, K. Schwarz, G. Madsen, D. Kvasnicka, and J. Luitz, *An Augmented Plane Wave Plus Local Orbitals Program for Calculating Crystal Properties* (Vienna University of Technology, Austria, 2001).
[35] J. P. Perdew, K. Burke, and M. Ernzerhof, Phys. Rev. Lett. **77**, 3865 (1996).
[36] G. K. H. Madsen and D. J. Singh, Comput. Phys. Commun. **175**, 67 (2006).
[37] A. van de Walle, M. Asta, and G. Ceder, Calphad **26**, 539 (2002).
[38] M. Heller and G. Danielson, J. Phys. Chem. Sol. **23**, 601 (1962).
[39] R. D. Redin, R. G. Morris, and G. C. Danielson, Phys. Rev. **109**, 1916 (1958).
[40] M. Yoshinaga, T. Iida, M. Noda, T. Endo, and Y. Takanashi, Thin Solid Films **461**, 86 (2004).
[41] G. A. Landrum, R. Hoffmann, J. Evers, and H. Boysen, Inorganic Chem. **37**, 5754 (1998).
[42] D. Parker and D. J. Singh, Sci. Tech. Adv. Mater. **14**, 055003 (2013).
[43] T. Nonomura, C. Wen, A. Kato, K. Isobe, Y. Kubota, T. Nakamura, M. Yamashita, Y. Hayakawa, and H. Tatsuoka, Phys. Procedia **11**, 110 (2011).
[44] T. Yamada and H. Yamane, Intermetallics **19**, 908 (2011).